A New Earthquake Location Method Based on the Waveform Inversion

Hao Wu[1], Jing Chen[1], Xueyuan Huang[2] and Dinghui Yang[1,*]

[1] *Department of Mathematical Sciences, Tsinghua University, Beijing 100084, China.*
[2] *Department of Mathematics, School of Science, Beijing Technology and Business University, Beijing 100048, China.*

Abstract. In this paper, a new earthquake location method based on the waveform inversion is proposed. As is known to all, the waveform misfit function under the L^2 measure is suffering from the cycle skipping problem. This leads to a very small convergence domain of the conventional waveform based earthquake location methods. In present study, by introducing and solving two simple sub-optimization problems, we greatly expand the convergence domain of the waveform based earthquake location method. According to a large number of numerical experiments, the new method expands the range of convergence by several tens of times. This allows us to locate the earthquake accurately even from some relatively bad initial values.

1   Introduction

The earthquake location is a fundamental problem in seismology [11, 31]. It consists of two parts: the determination of hypocenter ξ and origin time τ. These information are extremely important in quantitative seismology, e.g. the earthquake early warning system [28], the investigation of seismic heterogeneous structure [35, 37]. In particular, there are also significant interests in micro-earthquake which has many applications in exploration seismology [18, 26]. It also has a similar mathematical framework with the other source localization or source identification problems, e.g. [1, 4, 5, 23].

   Due to the importance of the earthquake location problem, numerous studies have been done theoretically and experimentally [11–13, 26, 30]. However, many studies are

---

*Corresponding author. *Email addresses:* `hwu@tsinghua.edu.cn` (H. Wu), `jing-che16@mails.tsinghua.edu.cn` (J. Chen), `huangxy.math10@gmail.com` (X. Y. Huang), `dhyang@math.tsinghua.edu.cn` (D. H. Yang)

based on the ray theory, which has low accuracy when the wave length is not small enough compared to the scale of wave propagating region [9,15,27,40]. This may lead to inaccurate or even incorrect earthquake location results. An alternative way is to solve the wave equation directly to get accurate waveform information for inversion. This method is becoming popular in recent years, as a result of the fast developing of computational power and techniques [14,16,19–21,29,34].

In the work by [21], see also [16], the spectral-element solvers are implemented to invert the basic information of earthquakes. The misfit functions defined based upon the envelope of the waveforms are minimized to provide the best estimation of source model parameters. Another approach proposed by [35] is based on the wave-field relation between the hypocenter ξ and its perturbation $\xi + \delta\xi$ [3]. Due to the foregoing observation, the travel-time differences between the synthetic signal and the real signal can be approximately expressed as the linear function of hypocenter perturbation $\delta\xi$. The authors then derived the sensitivity kernel by using the forward and adjoint wavefields.

However, the above mentioned papers on the earthquake location are not directly used the waveform difference since the waveform misfit function under the L^2 measure is suffering from the cycle skipping problem [21]. Consider the bad mathematical properties of the delta function $f(t-\tau)\delta(x-\xi)$, who is appeared as the source of wave equation, even small perturbation of hypocenter $\delta\xi$ and origin time $\delta\tau$ would generate large deviation of waveform. Thus, it is not surprising that the range of convergence of the conventional waveform based method is very small. On the other hand, the waveform signal may contain more information, which could lead to more accurate location result. Thus, it is necessary to develop new techniques to expand the convergence domain of the waveform based location method.

In this paper, we present a new method to locate the earthquake accurately. For the sake of simplicity, we use the acoustic wave equation and only deal with the earthquake hypocenter and origin time. There is no essential difficulty to consider the elastic wave equation or involve more earthquake information, e.g. the moment magnitudes [21]. The starting point is to keep $\frac{\|\delta s(x,t)\|}{\|s(x,t)\|} \ll 1$ in a modified sense. This is a fundamental assumption of the first-order Born approximation in the adjoint method. But it is not easy to guarantee in the classical sense, even if $\frac{\|\delta\xi\|}{\|\xi\|}$ and $\frac{\|\delta\tau\|}{\|\tau\|}$ are small. This is due to the bad mathematical properties of the delta function $f(t-\tau)\delta(x-\xi)$ in the wave equation. To solve this problem, we shift the synthetic data so that its difference with the real data is minimized. The shifting parameter can be obtained by solving a simple sub-optimization problem. The above effects ensure correctness of the important assumption $\frac{\|\delta s(x,t)\|}{\|s(x,t)\|} \ll 1$ of the adjoint method in a large range. Thus, we can expect a large convergence domain of the new earthquake location method. According to the numerical experiments, the range of convergence is significantly enlarged. We also remark that there have been many efforts in expanding the range of convergence for the inverse problem, see e.g. [8,10,24, 25,38]. Here we provide a simple and alternative implementation.

The paper is organized as follows. In Section 2, the conventional waveform based

adjoint inversion method is reviewed for the earthquake hypocenter and origin time. We propose the new method for the earthquake location in Section 3. In Section 4, the numerical experiments are provided to demonstrate the effectiveness of the new method. Finally, we make some conclusive remarks in Section 5.

2   The inversion method

Consider the scalar acoustic wave equation

$$\frac{\partial^2 u(\boldsymbol{x},t;\boldsymbol{\xi},\tau)}{\partial t^2} = \nabla \cdot \left(c^2(\boldsymbol{x}) \nabla u(\boldsymbol{x},t;\boldsymbol{\xi},\tau) \right) + f(t-\tau)\delta(\boldsymbol{x}-\boldsymbol{\xi}), \quad \boldsymbol{x},\boldsymbol{\xi} \in \Omega, \tag{2.1}$$

with initial-boundary conditions

$$u(\boldsymbol{x},0;\boldsymbol{\xi},\tau) = \partial_t u(\boldsymbol{x},0;\boldsymbol{\xi},\tau) = 0, \quad \boldsymbol{x} \in \Omega, \tag{2.2}$$

$$\boldsymbol{n} \cdot \left(c^2(\boldsymbol{x}) \nabla u(\boldsymbol{x},t;\boldsymbol{\xi},\tau) \right) = 0, \quad \boldsymbol{x} \in \partial\Omega. \tag{2.3}$$

Here $u(\boldsymbol{x},t;\boldsymbol{\xi},\tau)$ is the wavefield with respect to the origin time $\tau > 0$ and hypocenter $\boldsymbol{\xi} \in \Omega$. The wave speed is $c(\boldsymbol{x})$. The simulated domain $\Omega \subset \mathbb{R}^d$, d is the dimension of the problem and $\boldsymbol{n}$ is the unit outer normal vector to the boundary $\partial\Omega$ of Ω. The seismogram at source has the form of Ricker wavelet

$$f(t) = A \left(1 - 2\pi^2 f_0^2 t^2 \right) e^{-\pi^2 f_0^2 t^2}, \tag{2.4}$$

in which f_0 is the dominant frequency and A is the normalization factor. In this study, the point source hypothesis $\delta(\boldsymbol{x}-\boldsymbol{\xi})$ for the hypocenter focus is considered for the situation where the temporal and spatial scales of seismic rupture are extremely small compared to the scales of seismic waves propagated [2,22]. For simplicity, the free surface boundary condition (2.3) is considered here. There is no essential difference for other boundary conditions, e.g. the perfectly matched layer absorbing boundary condition [17].

Remark 2.1. For the acoustic wave equation (2.1), we have the invariance property in time translation

$$u(\boldsymbol{x},t-\Delta\tau;\boldsymbol{\xi},\tau) = u(\boldsymbol{x},t;\boldsymbol{\xi},\tau+\Delta\tau).$$

Remark 2.2. Accordingly to the compatibility condition of initial value, we require that

$$f(t-\tau) = 0, \quad \forall t \leq 0.$$

In our model, the Ricker wavelet $f(t)$ in (2.4) is exponential decay. The compatibility condition can be satisfied in an approximate sense by choosing a relative large τ. In practical problems, it is very natural to get.

Let $\boldsymbol{\xi}_T$ and τ_T be the real earthquake hypocenter and origin time. Thus, the real earthquake signal $d_r(t)$, which was recorded at receiver r can be considered as

$$d_r(t) = u(\boldsymbol{\eta}_r, t; \boldsymbol{\xi}_T, \tau_T). \tag{2.5}$$

Here $\boldsymbol{\eta}_r$ is the location of the $r-$th receiver. The synthetic signal $s(\boldsymbol{x}, t)$ corresponding to the initial hypocenter $\boldsymbol{\xi}$ and origin time τ is

$$s(\boldsymbol{x}, t) = u(\boldsymbol{x}, t; \boldsymbol{\xi}, \tau). \tag{2.6}$$

By introducing the misfit function

$$\chi_r(\boldsymbol{\xi}, \tau) = \frac{\int_0^T |d_r(t) - s(\boldsymbol{\eta}_r, t)|^2 \mathrm{d}t}{2 \int_0^T |d_r(t)|^2 \mathrm{d}t}, \tag{2.7}$$

we define the nonlinear optimization problem

$$(\boldsymbol{\xi}_T, \tau_T) = \underset{\boldsymbol{\xi}, \tau}{\operatorname{argmin}} \sum_r \chi_r(\boldsymbol{\xi}, \tau). \tag{2.8}$$

Obviously, the global solution exists and we believe in the uniqueness. In the following part, the sensitivity kernel [20, 27, 34] will be derived to solve this inversion problem iteratively.

2.1 The adjoint method

The perturbation of parameters $\frac{\|\delta\boldsymbol{\xi}\|}{\|\boldsymbol{\xi}\|}$ and $\frac{\|\delta\tau\|}{\|\tau\|} \ll 1$ would generate the perturbation of wave function $\delta s(\boldsymbol{x}, t)$, it writes

$$\delta s(\boldsymbol{x}, t) = u(\boldsymbol{x}, t; \boldsymbol{\xi} + \delta\boldsymbol{\xi}, \tau + \delta\tau) - u(\boldsymbol{x}, t; \boldsymbol{\xi}, \tau). \tag{2.9}$$

Then $\delta s(\boldsymbol{x}, t)$ satisfies

$$\begin{cases} \frac{\partial^2 \delta s(\boldsymbol{x}, t)}{\partial t^2} = \nabla \cdot \left(c^2(\boldsymbol{x}) \nabla \delta s(\boldsymbol{x}, t) \right) + f(t - (\tau + \delta\tau)) \delta(\boldsymbol{x} - (\boldsymbol{\xi} + \delta\boldsymbol{\xi})) \\ \qquad\qquad - f(t - \tau) \delta(\boldsymbol{x} - \boldsymbol{\xi}), & \boldsymbol{x} \in \Omega, \\ \delta s(\boldsymbol{x}, 0) = \frac{\partial \delta s(\boldsymbol{x}, 0)}{\partial t} = 0, & \boldsymbol{x} \in \Omega, \\ \boldsymbol{n} \cdot \left(c^2(\boldsymbol{x}) \nabla \delta s(\boldsymbol{x}, t) \right) = 0, & \boldsymbol{x} \in \partial\Omega. \end{cases} \tag{2.10}$$

Multiply an arbitrary test function $w_r(\boldsymbol{x}, t)$ on Eq. (2.10), integrate it on $\Omega \times [0, T]$ and use integration by parts, we obtain

$$\int_0^T \int_\Omega \frac{\partial^2 w_r}{\partial t^2} \delta s \, \mathrm{d}\boldsymbol{x} \mathrm{d}t - \int_\Omega \frac{\partial w_r}{\partial t} \delta s \Big|_{t=T} \mathrm{d}\boldsymbol{x} + \int_\Omega w_r \frac{\partial \delta s}{\partial t} \Big|_{t=T} \mathrm{d}\boldsymbol{x}$$

$$= \int_0^T \int_\Omega \delta s \nabla \cdot (c^2 \nabla w_r) \mathrm{d}\boldsymbol{x} \mathrm{d}t - \int_0^T \int_{\partial\Omega} \boldsymbol{n} \cdot (c^2 \nabla w_r) \delta s \, \mathrm{d}\zeta \mathrm{d}t$$

$$+ \int_0^T f(t - (\tau + \delta\tau)) w_r(\boldsymbol{\xi} + \delta\boldsymbol{\xi}, t) - f(t - \tau) w_r(\boldsymbol{\xi}, t) \mathrm{d}t$$

$$\approx \int_0^T \int_\Omega \delta s \nabla \cdot (c^2 \nabla w_r) \mathrm{d}\boldsymbol{x} \mathrm{d}t - \int_0^T \int_{\partial\Omega} \boldsymbol{n} \cdot (c^2 \nabla w_r) \delta s \mathrm{d}\zeta \mathrm{d}t$$

$$+ \int_0^T f(t-\tau)\nabla w_r(\boldsymbol{\xi},t) \cdot \delta\boldsymbol{\xi} - f'(t-\tau) w_r(\boldsymbol{\xi},t)\delta\tau \mathrm{d}t. \tag{2.11}$$

Note that the Taylor expansion is used and higher order terms are ignored in the last step.

On the other hand, the misfit function (2.7) also generates the perturbation with respect to $\delta s(\boldsymbol{x},t)$, assume that $\frac{\|\delta s(\boldsymbol{x},t)\|}{\|s(\boldsymbol{x},t)\|} \ll 1$, it writes

$$\delta\chi_r = \chi_r(\boldsymbol{\xi}+\delta\boldsymbol{\xi},\tau+\delta\tau) - \chi_r(\boldsymbol{\xi},\tau) = \frac{\int_0^T \left(|d_r(t)-(s+\delta s)(\boldsymbol{\eta}_r,t)|^2 - |d_r(t)-s(\boldsymbol{\eta}_r,t)|^2 \right)\mathrm{d}t}{2\int_0^T |d_r(t)|^2 \mathrm{d}t}$$

$$\approx -\frac{\int_0^T (d_r(t)-s(\boldsymbol{\eta}_r,t))\delta s(\boldsymbol{\eta}_r,t)\mathrm{d}t}{\int_0^T |d_r(t)|^2 \mathrm{d}t}$$

$$= -\frac{\int_0^T \int_\Omega (d_r(t)-s(\boldsymbol{\eta}_r,t))\delta s(\boldsymbol{x},t)\delta(\boldsymbol{x}-\boldsymbol{\eta}_r)\mathrm{d}\boldsymbol{x}\mathrm{d}t}{\int_0^T |d_r(t)|^2 \mathrm{d}t}, \tag{2.12}$$

where "$\approx$" is obtained by ignoring high order terms of $\delta s(\boldsymbol{x},t)$.

Let $w_r(\boldsymbol{x},t)$ satisfies the wave equation with terminal-boundary conditions

$$\begin{cases} \frac{\partial^2 w_r(\boldsymbol{x},t)}{\partial t^2} = \nabla \cdot \left(c^2(\boldsymbol{x})\nabla w_r(\boldsymbol{x},t)\right) + \frac{d_r(t)-s(\boldsymbol{\eta}_r,t)}{\int_0^T |d_r(t)|^2 \mathrm{d}t}\delta(\boldsymbol{x}-\boldsymbol{\eta}_r), & \boldsymbol{x}\in\Omega, \\ w_r(\boldsymbol{x},T) = \frac{\partial w_r(\boldsymbol{x},T)}{\partial t} = 0, & \boldsymbol{x}\in\Omega, \\ \boldsymbol{n}\cdot\left(c^2(\boldsymbol{x})\nabla w_r(\boldsymbol{x},t)\right) = 0, & \boldsymbol{x}\in\partial\Omega. \end{cases} \tag{2.13}$$

Thus, the linear relation for $\delta\chi_r$ and $\delta\boldsymbol{\xi}$, $\delta\tau$ can be obtained by subtracting (2.12) from (2.11)

$$-\delta\chi_r = \int_0^T f(t-\tau)\nabla w_r(\boldsymbol{\xi},t)\cdot\delta\boldsymbol{\xi} - f'(t-\tau)w_r(\boldsymbol{\xi},t)\delta\tau \mathrm{d}t. \tag{2.14}$$

In particular, if

$$\boldsymbol{\xi}+\delta\boldsymbol{\xi} = \boldsymbol{\xi}_T, \tau+\delta\tau = \tau_T,$$

it implies

$$\chi_r(\boldsymbol{\xi}+\delta\boldsymbol{\xi},\tau+\delta\tau) = 0 \implies \delta\chi_r = -\chi_r(\boldsymbol{\xi},\tau).$$

This gives an alternative form of equation (2.14)

$$\chi_r(\boldsymbol{\xi},\tau) = \int_0^T f(t-\tau)\nabla w_r(\boldsymbol{\xi},t)\cdot\delta\boldsymbol{\xi} - f'(t-\tau)w_r(\boldsymbol{\xi},t)\delta\tau \mathrm{d}t. \tag{2.15}$$

By defining the sensitivity kernel for the hypocenter $\boldsymbol{\xi}$ and origin time τ as

$$K_r^{\boldsymbol{\xi}} = \int_0^T \nabla w_r(\boldsymbol{\xi},t) f(t-\tau)\mathrm{d}t, \tag{2.16}$$

$$K_r^\tau = -\int_0^T w_r(\boldsymbol{\xi},t) f'(t-\tau)\mathrm{d}t, \tag{2.17}$$

Eq. (2.15) gives a single equation of the linear system

$$\frac{K_r^{\xi}}{\chi_r(\xi,\tau)}\cdot\delta\xi+\frac{K_r^{\tau}}{\chi_r(\xi,\tau)}\delta\tau=1. \tag{2.18}$$

The above linear system has been normalized so that the condition number can be optimized

2.2 The wave-equation-based traveltime inversion

The above discussions lead to the waveform based earthquake location method. Taking into account that the traveltime information can be more easily obtained in practice, we now turn to the derivation of the wave-equation based traveltime inversion for earthquake's hypocenter and origin time.

First, we define the traveltime misfit function as follows

$$\widetilde{\chi}_r(\xi,\tau)=\frac{1}{2}\left(T_r^{obs}-T_r^{syn}\right)^2, \tag{2.19}$$

here T_r^{obs} and T_r^{syn} are the observed traveltime which can be extracted from the real earthquake signal $d_r(t)$ and the synthetic signal $s(\eta_r,t)$. Correspondingly, the nonlinear optimization problem is defined as

$$(\xi_T,\tau_T)=\operatorname*{argmin}_{\xi,\tau}\sum_r\widetilde{\chi}_r(\xi,\tau). \tag{2.20}$$

Next, we need to derive the Fréchet derivatives of the optimization problem (2.20). Similar to the previous Subsection, the perturbation of wave function $\delta s(x,t)$ in (2.9) is generated by the perturbation of parameters $\frac{\|\delta\xi\|}{\|\xi\|}$ and $\frac{\|\delta\tau\|}{\|\tau\|}\ll 1$. Further assume that $\frac{\|\delta s(x,t)\|}{\|s(x,t)\|}\ll 1$, the relation between the traveltime shift δT_r^{syn} and the wave function perturbation $s(x,t)$ can be written as

$$\delta T_r^{syn}=\frac{1}{N_r}\int_0^T v(t)\partial_t s(\eta_r,t)\delta s(\eta_r,t)\mathrm{d}t, \tag{2.21}$$

$$N_r=\int_0^T v(t)s(\eta_r,t)\partial_t^2 s(\eta_r,t)\mathrm{d}t. \tag{2.22}$$

Here $v(t)$ is a time window over the time interval $[0,T]$, that can be used to pickup specific seismic phase. The detailed derivation can be found in [7, 34, 35]. Thus, the perturbation of the misfit function $\delta\widetilde{\chi}_r$ satisfies

$$\delta\widetilde{\chi}_r=\widetilde{\chi}_r(\xi+\delta\xi,\tau+\delta\tau)-\widetilde{\chi}_r(\xi,\tau)=\frac{1}{2}(T_r^{obs}-(T_r^{syn}+\delta T_r^{syn}))^2-\frac{1}{2}(T_r^{obs}-T_r^{syn})^2$$

$$\approx-\delta T_r^{syn}(T_r^{obs}-T_r^{syn})=-\frac{T_r^{obs}-T_r^{syn}}{N_r}\int_0^T v(t)\partial_t s(\eta_r,t)\delta s(\eta_r,t)\mathrm{d}t,$$

$$=-\frac{T_r^{obs}-T_r^{syn}}{N_r}\int_0^T\int_\Omega v(t)\partial_t s(\eta_r,t)\delta s(x,t)\delta(x-\eta_r)\mathrm{d}x\mathrm{d}t, \tag{2.23}$$

where "$\approx$" is obtained by ignoring high order terms of δT_r^{syn}.

Let $w_r(\boldsymbol{x},t)$ in (2.11) satisfies the wave equation with terminal-boundary conditions

$$\begin{cases} \frac{\partial^2 w_r(\boldsymbol{x},t)}{\partial t^2} = \nabla \cdot \left(c^2(\boldsymbol{x}) \nabla w_r(\boldsymbol{x},t) \right) + \frac{T_r^{obs} - T_r^{syn}}{N_r} \nu(t) \partial_t s(\boldsymbol{\eta}_r,t) \delta(\boldsymbol{x} - \boldsymbol{\eta}_r), & \boldsymbol{x} \in \Omega, \\ w_r(\boldsymbol{x},T) = \frac{\partial w_r(\boldsymbol{x},T)}{\partial t} = 0, & \boldsymbol{x} \in \Omega, \\ \boldsymbol{n} \cdot \left(c^2(\boldsymbol{x}) \nabla w_r(\boldsymbol{x},t) \right) = 0, & \boldsymbol{x} \in \partial\Omega. \end{cases} \quad (2.24)$$

Thus, the linear relation for $\delta\widetilde{\chi}_r$ and $\delta\boldsymbol{\xi}$, $\delta\tau$ can be obtained by subtracting (2.23) from (2.11)

$$-\delta\widetilde{\chi}_r = \int_0^T f(t-\tau) \nabla w_r(\boldsymbol{\xi},t) \cdot \delta\boldsymbol{\xi} - f'(t-\tau) w_r(\boldsymbol{\xi},t) \delta\tau \, \mathrm{d}t. \quad (2.25)$$

By a similar discussion as used in Subsection 2.1, we obtain the similar linear system

$$\frac{K_r^{\boldsymbol{\xi}}}{\widetilde{\chi}_r(\boldsymbol{\xi},\tau)} \cdot \delta\boldsymbol{\xi} + \frac{K_r^{\tau}}{\widetilde{\chi}_r(\boldsymbol{\xi},\tau)} \delta\tau = 1 \quad (2.26)$$

with the similar sensitivity kernel define in (2.16)-(2.17). The difference lies in that $w_r(\boldsymbol{\xi},t)$ satisfies the wave equation with terminal-boundary conditions (2.24).

3   A new method to expand the convergence domain

In this section, we are investigating the techniques to enlarge the convergence domain for the inversion of earthquake hypocenter $\boldsymbol{\xi}_T$ and origin time τ_T. It is assumed that the wave speed $c(\boldsymbol{x})$ is already well known. For situations of inaccurate or unknown wave speed, we refer to the discussions in [21] or the joint inversion for wave speed, hypocenter and origin time. We also remark that the following discussions are based on the framework of waveform inversion. But there is no significant difference for the wave-equation-based traveltime inversion.

3.1   Estimation of the origin time

As it was discussed in Section 2.1, the first-order Born approximation in the adjoint method requires an infinitesimal perturbation assumption of wave function

$$\frac{\|\delta s(\boldsymbol{x},t)\|}{\|s(\boldsymbol{x},t)\|} \ll 1,$$

see also [20, 27, 34, 36]. However, as we will see in Example 3.1, it is very difficult to guarantee this assumption even if the perturbations of the earthquake hypocenter and origin time are very small

$$\frac{\|\delta\boldsymbol{\xi}\|}{\|\boldsymbol{\xi}\|} \ll 1 \quad \text{and} \quad \frac{\|\delta\tau\|}{\|\tau\|} \ll 1.$$

That's one of the reasons why the convergence domain of the waveform based method is very small.

Example 3.1. This is a 2D unbounded problem with constant wave speed $c(x) \equiv c_0$ for the scalar acoustic wave equation (2.1) with initial condition (2.2). Its solution can be analytically given:

$$u(x,t;\boldsymbol{\xi},\tau) = \begin{cases} \frac{1}{2\pi c_0^2} \int_0^{\theta_0} \frac{f(\theta-\tau)}{\sqrt{(t-\theta)^2-(t-\theta_0)^2}} d\theta, & \theta_0 > 0, \\ 0, & \theta_0 \leq 0, \end{cases} \tag{3.1}$$

in which

$$\theta_0 = t - \frac{1}{c_0} \|x - \boldsymbol{\xi}\|_2.$$

Let $x = (x,z)$ denote the horizontal and depth coordinate respectively. The constant wave speed is $c_0 = 6.5 km/s$. There are 20 equidistant receivers on the surface,

$$\boldsymbol{\eta}_r = (x_r,z_r) = (5r - 2.5km,0), \quad r = 1,2,\cdots,20.$$

Consider an earthquake occurs at hypocenter $\boldsymbol{\xi}_T = (50km,30km)$ and origin time $\tau_T = 10s$ with dominant frequency $f_0 = 2$Hz, its signal $d_r(t)$ received by receiver $r = 7$ can be considered as (2.5) and (3.1). The synthetic signal $s(\boldsymbol{\eta}_r,t)$ corresponding to the initial hypocenter $\boldsymbol{\xi} = (52km,30.3km)$ and origin time $\tau = 10s$ at the same receiver $r = 7$ can be obtained by (2.6) and (3.1). The perturbation between the real and initial hypocenter is small

$$\delta\boldsymbol{\xi} = \boldsymbol{\xi}_T - \boldsymbol{\xi} = (-2km, -0.3km),$$

and it is also correct for the perturbation between the real and initial origin time

$$\delta\tau = \tau_T - \tau = 0.$$

Nevertheless, as we can see in Fig. 1, the difference between the real signal $d_r(t)$ and the synthetic signal $s(\boldsymbol{\eta}_r,t)$ at receiver $r = 7$ is significantly large:

$$\frac{\|d_r(t) - s(\boldsymbol{\eta}_r,t)\|}{\|d_r(t)\|} \sim 1,$$

which contracts to the basic assumption.

The key observation in Example 3.1 is that the infinitesimal perturbation assumption $\frac{\|\delta s(x,t)\|}{\|s(x,t)\|} \ll 1$ is not trivial to get. However, we note that the main difference between the real signal $d_r(t)$ and synthetic signal $s(\boldsymbol{\eta}_r,t)$ is caused by the time shift. Thus, we define the relative error function with respect to the time shift of the synthetic signal

$$e_r(\tau) = \frac{\|d_r(t) - s(\boldsymbol{\eta}_r,t-\tau)\|}{\|d_r(t)\|}. \tag{3.2}$$
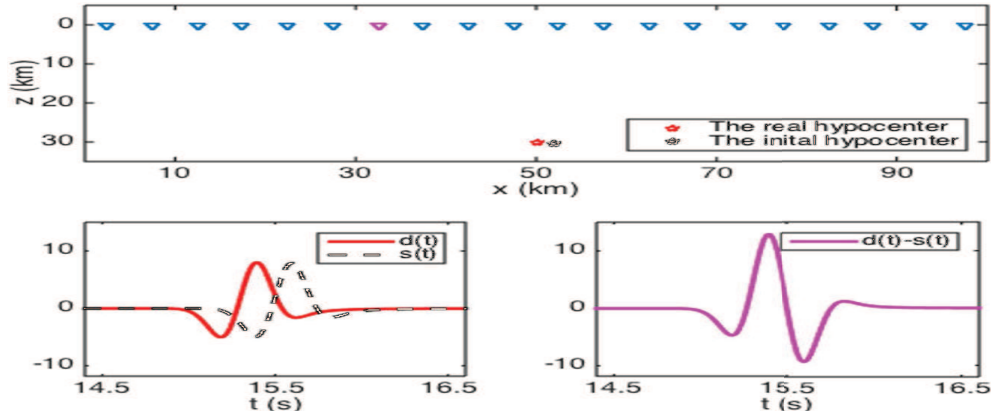
Figure 1: Illustration of Example 3.1. Top: The receivers (inverted triangle, magenta for $r=7$ and blue for others), the real (red pentagram) and initial hypocenter (black pentagram). Bottom Left: The real signal $d_r(t)$ (red solid line) and the synthetic signal $s(\eta_r, t)$ (black dashed line) at receiver $r=7$. Bottom Right: The difference between the real and synthetic signal $d_r(t) - s(\eta_r, t)$ (magenta solid line) at receiver $r=7$. The text representation in the figure has been simplified without causing any misunderstandings.

Solving the following sub-optimization problem

$$\tau_r^* = \underset{\tau}{\operatorname{argmin}}\, e_r(\tau), \tag{3.3}$$

the infinitesimal perturbation assumption may be satisfied in the sense of time translation.

$$\frac{\|d_r(t) - s(\eta_r, t - \tau_r^*)\|}{\|d_r(t)\|} \ll 1. \tag{3.4}$$

Example 3.2. Consider the same parameters set up as in Example 3.1, thereby the real signal $d_r(t)$ and the synthetic signal $s(\eta_r, t)$ are the same as those in Example 3.1.

The relative error function $e_r(\tau)$ defined in (3.2) is presented in Fig. 2(top). We can observe a global minimum of $e_r(\tau)$. Thus, the optimal time translation parameter τ_r^* can be easily computed through (3.3).

According to the above time translation, the difference between the real signal $d_r(t)$ and the shifted synthetic signal $s(\eta_r, t - \tau_r^*)$ is small, see Fig. 2(bottom). This implies that the modified infinitesimal perturbation assumption in (3.4) is satisfied here.

At last, by the invariance property in time translation, see Remark 2.1, this optimal time shift τ_r^* computed from (3.3) can be used to shift the initial origin time

$$\hat{\tau} = \tau + \tau_r^*, \tag{3.5}$$

so that the infinitesimal perturbation assumption $\frac{\|\delta s(x,t)\|}{\|s(x,t)\|} \ll 1$ can be satisfied in the original sense rather than the modified sense (3.4).
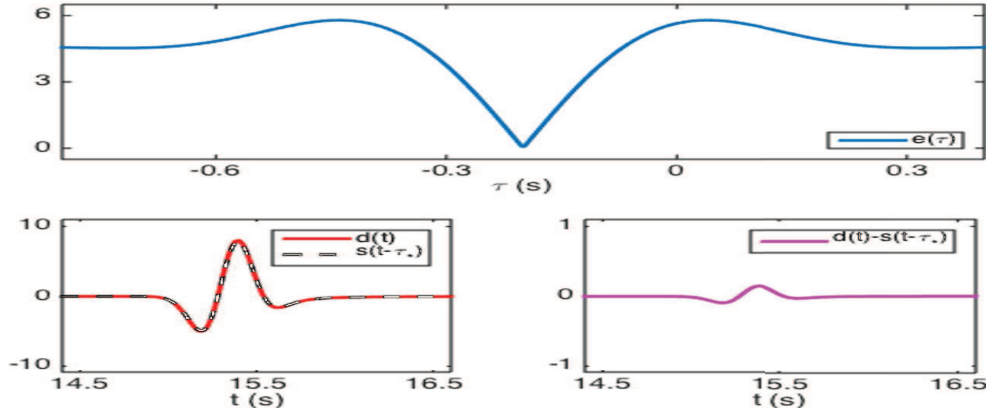
Figure 2: Illustration of Example 3.2. Top: The relative error function $e_r(\tau)$ defined in (3.2). Bottom Left: The real signal $d_r(t)$ (red solid line) and the shifted synthetic signal $s(\eta_r, t - \tau_r^*)$ (black dashed line) at receiver $r=7$. Bottom Right: The difference between the real signal and the shifted synthetic signal $d_r(t) - s(\eta_r, t - \tau_r^*)$ (magenta solid line) at receiver $r=7$. The text representation in the figure has been simplified without causing any misunderstandings.

Example 3.3. Consider the same parameters set up as in Example 3.1, thereby the real signal $d_r(t)$ is the same as in Example 3.1. The synthetic signals are corresponding to the initial hypocenter $\xi = (52km, 30.3km)$ and two different initial origin time: (1) $\tau_1 = 10$s, (2) $\tau_2 = \tau_1 + \tau_r^*$. We still focus on the signals received at receiver $r=7$. These synthetic signals can be obtained by

$$s_1(\eta_r, t) = u(\eta_r, t; \xi, \tau_1), \quad s_2(\eta_r, t) = u(\eta_r, t; \xi, \tau_2).$$

In Fig. 3(top), the difference between the real signal $d_r(t)$ and the synthetic signal $s_1(\eta_r, t)$ is large, but the difference between the real signal $d_r(t)$ and the other synthetic signal $s_2(\eta_r, t)$ is small, see Fig. 3(bottom).

3.2   The selection of receivers

In previous subsection, the time shift τ_r^* has been discussed for single receiver r. For practical problems, there are many receivers, thus we need to solve the following sub-optimization problem

$$\tau^* = \underset{\tau}{\text{argmin}} \sum_{r \in \mathcal{R}} e_r(\tau), \tag{3.6}$$

rather than (3.3). Here $\mathcal{R}$ is the set of all receivers that we use for inversion, which will be determined later. The set of all receivers is denote by $\mathcal{A}$, and it is obviously that $\mathcal{R} \subset \mathcal{A}$.

Example 3.4. Consider the same parameters set up as in Example 3.1, thereby the real signals $d_r(t)$ and the synthetic signals $s(\eta_r, t)$ can be obtained in the same manner as in Example 3.1

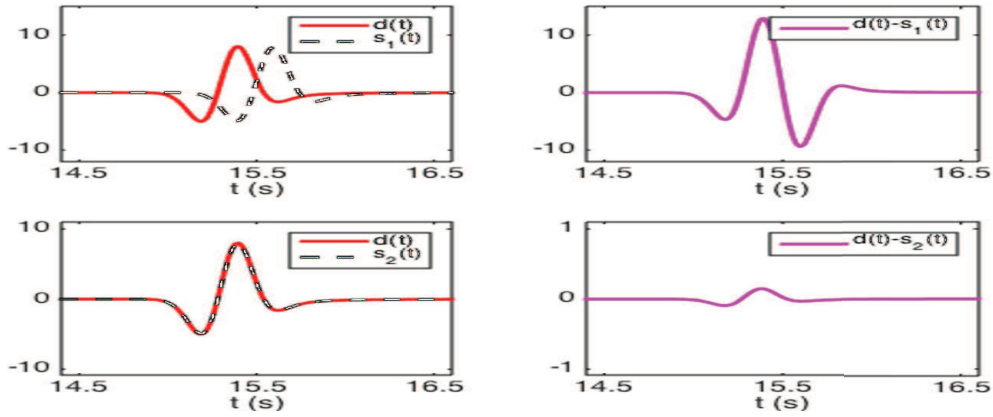$$d_r(t) = u(\eta_r, t; \xi_T, \tau_T), \quad s(\eta_r, t) = u(\eta_r, t; \xi, \tau)$$

Figure 3: Illustration of Example 3.3. Left: The real signal $d_r(t)$ (red solid line) and the synthetic signal $s_i(t, \eta_r)$ (black dashed line) at receiver $r=7$. Right: The difference between the real signal and the synthetic signal $d_r(t) - s_i(\eta_r, t)$ (magenta solid line) at receiver $r=7$. Top: $i=1$, which corresponding to the initial origin time τ_1. Bottom: $i=2$, which corresponding to the other initial origin time τ_2. The text representation in the figure has been simplified without causing any misunderstandings.
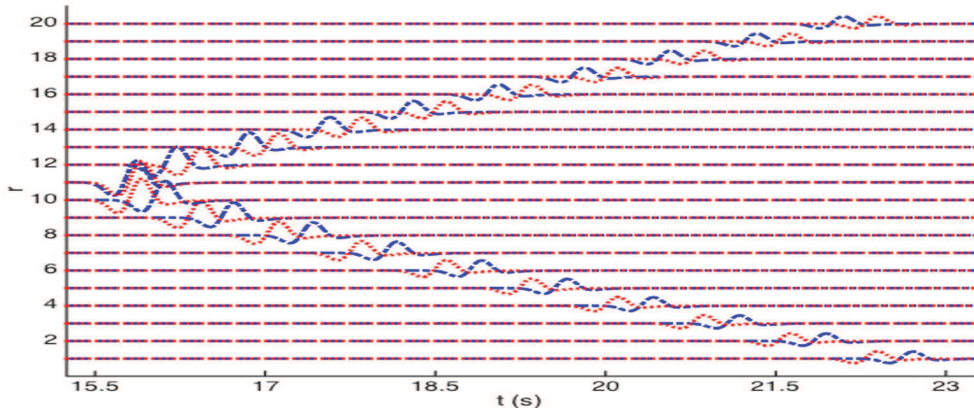
Figure 4: Illustration of Example 3.4. The waveform comparison of real signals $d_r(t)$ (red dotted line) and the synthetic signals $s(\eta_r, t)$ (blue dashdot line) for all receivers $r=1, 2, \cdots, 20$. The horizontal axis is the time t, and the longitudinal axis is the index of receiver r.

for all receivers $r \in \mathcal{A} = \{1, 2, \cdots, 20\}$. In Fig. 4, we output all the real signals $d_r(t)$ and the synthetic signals $s(\eta_r, t)$. According to the figures, we can see that

$$\tau_r^* < 0, \quad \text{for } r = 1, 2, \cdots, 10,$$
$$\tau_r^* > 0, \quad \text{for } r = 11, 12, \cdots, 20.$$

Therefore, we cannot get satisfactory value τ^* from (3.6) if $\#\mathcal{R}$ is large. Here $\#\mathcal{R}$ denotes the number of elements in the set $\mathcal{R}$.

The above example shows that discussions in Subsection 3.1 may fail when $\#\mathcal{R}$ is large. In fact, due to the small degree of freedom of the earthquake location problem, it is

not necessary to consider large $\#\mathcal{R}$. On the other hand, $\#\mathcal{R}$ is the number of constraints, which is proportional to the number of wave field computations. Therefore, we prefer to choose a relative small $\#\mathcal{R}$ for inversion. Accordingly to our numerical experiences, a suitable choice of $\#\mathcal{R}$ is $5\sim7$. However, this discussion doesn't determine which elements should be in $\mathcal{R}$. A natural consideration is to solve a more general nonlinear optimization problem

$$(\tau^*,\mathcal{R}^*)=\operatorname*{argmin}_{\tau,\mathcal{R}\subset\mathcal{A}}\sum_{r\in\mathcal{R}}e_r(\tau). \tag{3.7}$$

The essence of the above problem is that receivers set $\mathcal{R}$ is considered as optimization variable. It is easy to check that for $1\leq n_1<n_2\leq\#\mathcal{A}$, we have

$$\min_{\tau,\#\mathcal{R}=n_1,\mathcal{R}\subset\mathcal{A}}\sum_{r\in\mathcal{R}}e_r(\tau)\leq\min_{\tau,\#\mathcal{R}=n_2,\mathcal{R}\subset\mathcal{A}}\sum_{r\in\mathcal{R}}e_r(\tau).$$

In practice, solving the problem (3.7) is complicated. Instead, we can firstly solve a simplified optimization problem

$$(\bar{\tau},\mathcal{R}^*)=\operatorname*{argmin}_{\tau,\mathcal{R}\subset\mathcal{A}}\sum_{r\in\mathcal{R}}|\tau_r^*-\tau|^2. \tag{3.8}$$

Then, for fixed receivers set $\mathcal{R}^*$, we have

$$\tau^*=\operatorname*{argmin}_{\tau}\sum_{r\in\mathcal{R}^*}e_r(\tau). \tag{3.9}$$

Similar to Eq. (3.5), the optimal time shift τ^* for multiple receivers can also be used to shift the initial origin time

$$\hat{\tau}=\tau+\tau^*. \tag{3.10}$$

3.3 The detailed implementation

In summary of all the above, the detailed implementation of the algorithm is as follows:

1. Initialization. Set the tolerance value $\varepsilon=0.01km$, the threshold value $\sigma=100km$ and the break-off step $K=30$. Let $k=0$ and give the initial hypocenter ξ_0 and the initial origin time $\tau_0=0$.

2. For ξ_k, solving (3.8) to determine the receivers set $\mathcal{R}_k^*$ and estimating the origin time τ_k by (3.9) and (3.10).

3. Construct the sensitivity kernels $K_{r,k}^{\xi}$, $K_{r,k}^{\tau}$ for $r\in\mathcal{R}_k^*$ and solve the normalized linear system (2.18) to get $\delta\xi_k$ and $\delta\tau_k$, then update the estimation of hypocenter for step $k+1$,

$$\xi_{k+1}=\xi_k+\delta\xi_k.$$

4. If $\left\|\xi_k-\xi_{k+1}\right\|<\varepsilon$, go to step 7; If $\left\|\xi_k-\xi_{k+1}\right\|>\sigma$, go to step 6.

5. If $k+1 > K$, go to step 6. Otherwise, let $k = k+1$ and go to step 2 for another iteration.

6. Output the error message: "The iteration diverges." and stop.

7. Update the estimation of origin time for step $k+1$,

$$\tau_{k+1} = \tau_k + \delta\tau_k.$$

Output (ξ_{k+1}, τ_{k+1}) and stop.

Once the value (ξ_{k+1}, τ_{k+1}) is output, we get the hypocenter and the origin time for the specific earthquake. Otherwise, the algorithm should be restarted with different initial value of hypocenter ξ_0 until the convergent result is obtained.

In this algorithm, the extra computational cost arise from solving the sub-optimization problem (3.8) and (3.9). But this part in the overall computational cost is minor. The reason is that the sub-optimization problem (3.8) and (3.9) are only one dimensional. Taking into consideration the saving from less computation of the wave equations, the total cost is reduced here. Furthermore, since the new method greatly enlarges the convergence domain, the number of initial values of hypocenter that we need to select in solving the earthquake location problem can be significantly reduced compared to the conventional method. This greatly reduces the overall computational cost.

4   Numerical experiments

In this section, three examples are presented to demonstrate the validity of our method. And we will see the comparison between the conventional method and the new method for the earthquake location problem.

Example 4.1. Let's take the same parameters set up as in Example 3.1. Then the real signals $d_r(t)$ and the synthetic $s(\eta_r, t)$ can be obtained by (2.5), (2.6) and (3.1) for different receiver $r = 1, 2, \cdots, 20$.

Consider an earthquake occurs at hypocenter $\xi_T = (50km, 30km)$ and origin time $\tau_T = 10s$ with dominant frequency $f_0 = 2$Hz. In Fig. 5(top left), 2800 uniformly distributed grid nodes are tested as the initial hypocenter of earthquake ξ in the searching domain $[10km, 90km] \times [0km, 70km]$ for the conventional method. There are 22 grid nodes converge to the correct hypocenter. For the new method, there are 1597 grid nodes converge to the correct hypocenter in the same set-up, see Fig. 5(top right). In contrast, the convergence probability of the new method is about 72 times that of the conventional method. From the figure, we can also see that all the tested initial hypocenter in the rectangular region $[48km, 52km] \times [28km, 32km]$ converge to the correct hypocenter for the conventional method. For the new method, this rectangular region is $[38km, 62km] \times [7.5km, 53.5km]$, its area is about 75 times of the former.

Consider an earthquake occurs at hypocenter $\xi_T = (50km, 6km)$ and origin time $\tau_T = 10s$ with dominant frequency $f_0 = 2$Hz. In Fig. 5(bottom left), 1900 uniformly distributed
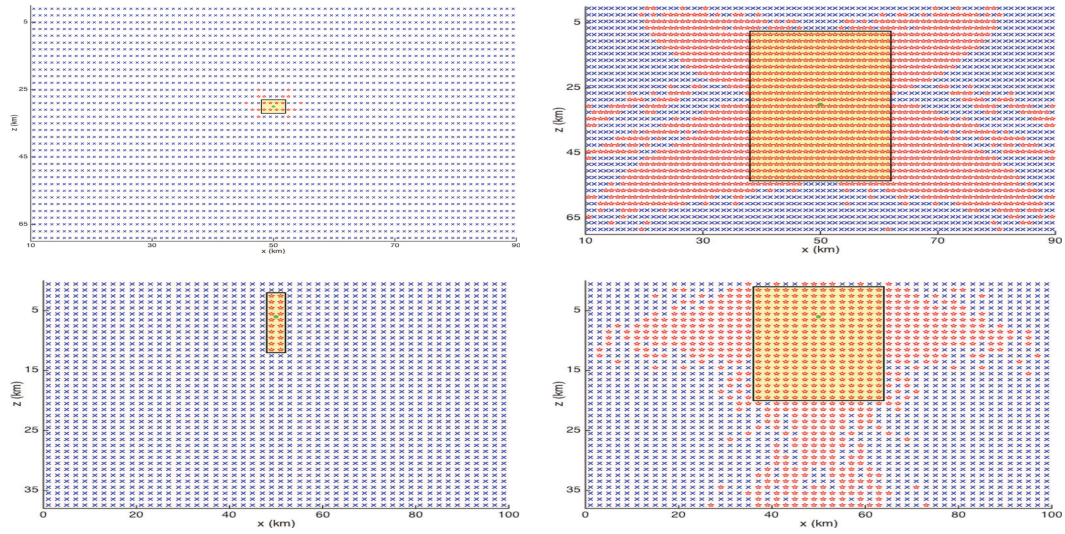
Figure 5: Illustration of the Example 4.1. The green point is the real hypocenter. The red pentagram and the blue x-mark indicate the initial hypocenter at this location converge and misconvergence to the real hypocenter respectively. Left: the conventional method; Right: the new method. Top figures for deep earthquake $\zeta_T = (50km, 30km)$ and bottom figures for shallow earthquake $\zeta_T = (50km, 6km)$. In the light yellow rectangular region, all the tested initial hypocenter converge to the correct hypocenter.

grid nodes are tested as the initial hypocenter of earthquake ζ in the searching domain $[0km, 100km] \times [0km, 38km]$ for the conventional method. There are 20 grid nodes converge to the correct hypocenter. For the new method, there are 740 grid nodes converge to the correct hypocenter in the same set-up, see Fig. 5(bottom right). In contrast, the convergence probability of the new method is about 37 times that of the conventional method. From the figure, we can also see that all the tested initial hypocenter in the rectangular region $[48km, 52km] \times [2km, 12km]$ converge to the correct hypocenter for the conventional method. For the new method, this rectangular region is $[36km, 64km] \times [1km, 20km]$, its area is about 13 times of the former.

Considering all of the above, we note that the new method works better for the deep earthquake rather than the shallow earthquake. One explanation is that the convergence domain is nearly symmetric about the earthquake hypocenter. But it doesn't hold for shallow earthquake in z direction since selecting the initial hypocenter above the surface is non-physical. This discussion also applies to the following examples.

Example 4.2. Consider the two-layer model in the bounded domain $[0km, 100km] \times [0km, 40km]$, the wave speed is

$$c(x,z) = \begin{cases} 5.2 + 0.06z + 0.2\sin\frac{\pi x}{25}, & 0km \leq z \leq 15km, \\ 6.2 + 0.2\sin\frac{\pi x}{25}, & 15km < z \leq 40km, \end{cases}$$

for depth earthquake and

$$c(x,z) = \begin{cases} 5.2+0.05z+0.2\sin\frac{\pi x}{25}, & 0km \leq z \leq 20km, \\ 6.8+0.2\sin\frac{\pi x}{25}, & 20km < z \leq 40km, \end{cases}$$

for shallow earthquake. The unit is 'km/s'. We use the finite difference scheme [6,41] to solve the acoustic wave equation (2.1) with initial condition (2.2). The free surface boundary condition is used on the earth's surface, and the perfectly matched layer [17] is used for other boundaries. The delta function $\delta(x-\xi)$ in the wave equation (2.1) is discretized using the techniques proposed in [39].

$$\delta(x) = \begin{cases} \frac{1}{h}\left(1-\frac{5}{4}\left|\frac{x}{h}\right|^2-\frac{35}{12}\left|\frac{x}{h}\right|^3+\frac{21}{4}\left|\frac{x}{h}\right|^4-\frac{25}{12}\left|\frac{x}{h}\right|^5\right), & |x| \leq h, \\ \frac{1}{h}\left(-4+\frac{75}{4}\left|\frac{x}{h}\right|-\frac{245}{8}\left|\frac{x}{h}\right|^2+\frac{545}{24}\left|\frac{x}{h}\right|^3-\frac{63}{8}\left|\frac{x}{h}\right|^4+\frac{25}{24}\left|\frac{x}{h}\right|^5\right), & h < |x| \leq 2h, \\ \frac{1}{h}\left(18-\frac{153}{4}\left|\frac{x}{h}\right|+\frac{255}{8}\left|\frac{x}{h}\right|^2-\frac{313}{24}\left|\frac{x}{h}\right|^3+\frac{21}{8}\left|\frac{x}{h}\right|^4-\frac{5}{24}\left|\frac{x}{h}\right|^5\right), & 2h < |x| \leq 3h, \\ 0, & |x| > 3h. \end{cases}$$

There are 20 equidistant receivers on the surface

$$\eta_r = (x_r, z_r) = (5r-2.5km, 0), \quad r = 1,2,\cdots,20.$$

Since the hypocenter of earthquake is not far from the receivers, we only use the direct wave to locate the earthquake.

Consider an earthquake occurs below the medium interface $\xi_T = (50km, 20km)$ and origin time $\tau_T = 10s$ with dominant frequency $f_0 = 2$Hz (see Fig. 6(top)). In Fig. 7(top left), 1480 uniformly distributed grid nodes are tested as the initial hypocenter of earthquake ξ in the searching domain $[10km, 90km] \times [0km, 40km]$ for the conventional method. There are 38 grid nodes converge to the correct hypocenter. For the new method, there are 881 grid nodes converge to the correct hypocenter in the same set-up, see Fig. 7(top right). In contrast, the convergence probability of the new method is about 23 times that of the conventional method. From the figure, we can also see that all the tested initial hypocenter in the rectangular region $[47km, 53km] \times [17.4km, 22.6km]$ converge to the correct hypocenter for the conventional method. For the new method, this rectangular region is $[33km, 67km] \times [5.5km, 33.5km]$, its area is about 30 times of the former.

Consider an earthquake occurs above the medium interface $\xi_T = (50km, 6km)$ and origin time $\tau_T = 10s$ with dominant frequency $f_0 = 2$Hz (see Fig. 6(bottom)). In Fig. 7(bottom left), 1344 uniformly distributed grid nodes are tested as the initial hypocenter of earthquake ξ in the searching domain $[8km, 92km] \times [0km, 25km]$ for the conventional method. There are 68 grid nodes converge to the correct hypocenter. For the new method, there are 592 grid nodes converge to the correct hypocenter in the same set-up, see Fig. 7(bottom right). In contrast, the convergence probability of the new method is about 9 times that of the conventional method. From the figure, we can also see that all the tested initial hypocenter in the rectangular region $[48km, 52km] \times [0.8km, 15.8km]$ converge to the
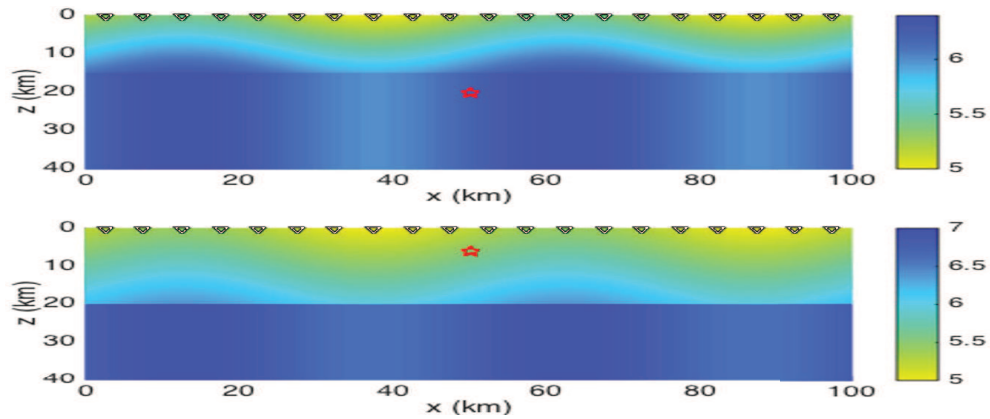
Figure 6: Velocity models in Example 4.2. The red pentagrams show the hypocenter of earthquake and the black triangles indicate the receivers.
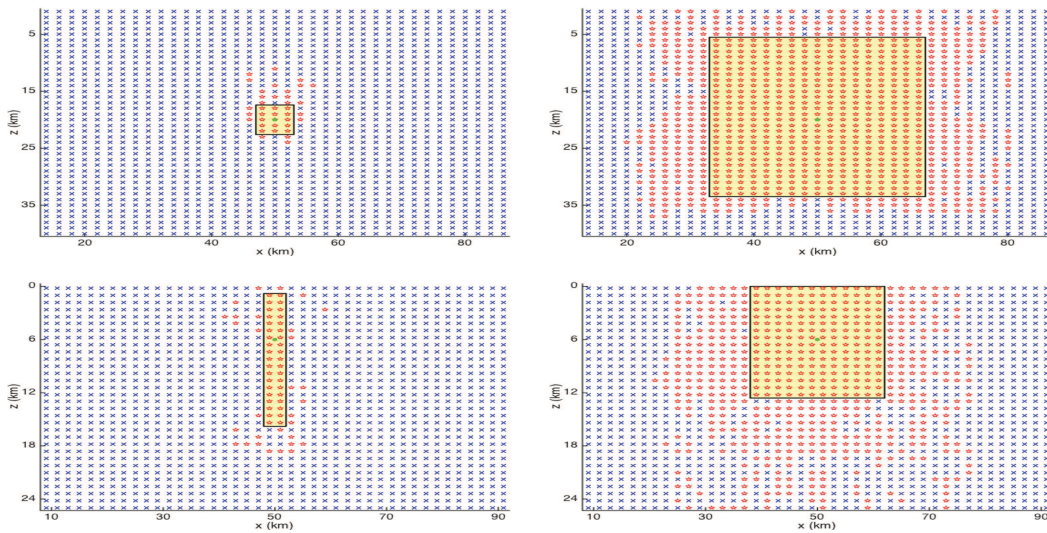

Figure 7: Illustration of the Example 4.2. The green point is the real hypocenter. The red pentagram and the blue x-mark indicate the initial hypocenter at this location converge and misconvergence to the real hypocenter respectively. Left: the conventional method; Right: the new method. Top figures for deep earthquake $\xi_T = (50km,20km)$ and bottom figures for shallow earthquake $\xi_T = (50km,6km)$. In the light yellow rectangular region, all the tested initial hypocenter converge to the correct hypocenter.

correct hypocenter for the conventional method. For the new method, this rectangular region is $[38km,62km] \times [0km,12.6km]$, its area is about 5 times of the former.

Remark 4.1. In Example 4.1 and Example 4.2, we can observe a large convergence domain of our new method, see Fig. 5(right) and Fig. 7(right). On the other hand, the ray theory based earthquake location method, e.g. the Geiger's method, may provide close locating results. If we use the ray theory based earthquake location method to provide

an initial hypocenter for our new method, we may expect a much larger convergence domain.

Example 4.3. Consider the velocity model consisting of the crust and the mantle, containing an undulated Moho discontinuity and a subduction zone with a thin low velocity layer atop a fast velocity layer [35], see Fig. 8 for illustration. The computational domain is $[0km, 200km] \times [0km, 200km]$, and the wave speed is

$$
c(x,z) = \begin{cases}
5.5, & 0 < z \le 33 + 2.5\sin\frac{\pi x}{40}, \\
7.8, & 33 + 2.5\sin\frac{\pi x}{40} < z \le 45 + 0.4x, \\
7.488, & 45 + 0.4x < z \le 60 + 0.4x, \\
8.268, & 60 + 0.4x < z \le 100 + 0.4x, \\
7.8, & \text{others.}
\end{cases}
$$

with unit 'km/s'. We consider the same set-up as in Example 4.2, e.g. the forward scheme, the boundary conditions and the discretized delta function. There are 12 receivers $\eta_r = (x_r, z_r)$ on the surface with $z_r = 0$, their horizontal positions are randomly given, see Table 1 for details. In this example, we still only use the direct wave to locate the earthquake. In real world, region with the similar velocity model is always seismogenic zone [32]. Earthquakes in this kind of region can occur in the crust, in the subduction zone or in the mantle [33]. Complex velocity structure makes source location very difficult.

Table 1: Example 4.3: the horizontal positions of receivers, with unit 'km'.

r	1	2	3	4	5	6	7	8	9	10	11	12
x_r	21	33	39	58	68	74	86	98	126	132	158	197

We firstly investigate the case that the earthquake occurs in the mantle but the initial hypocenter of the earthquake is chosen in the subduction zone, and its contrary case. In Fig. 9, we can see the convergent history. The second case is that the earthquake occurs in the mantle but the initial hypocenter of the earthquake is chosen in the crust. The convergent history can be seen in Fig. 10. From these tests, we can observe nice convergent result of the new method, even though the real and initial hypocenter of the earthquakes are far from each other.

Example 4.4. In this example, we test the influences of the data noise and inaccurate velocity model. The computational domain is $[0km, 100km] \times [0km, 40km]$, and the wave speed is

$$
c(x,z) = \begin{cases}
5.2 + 0.06z + 0.2\sin\frac{\pi x}{25}, & 0km \le z \le 15km, \\
6.2 + 0.2\sin\frac{\pi x}{25}, & 15km < z \le 40km,
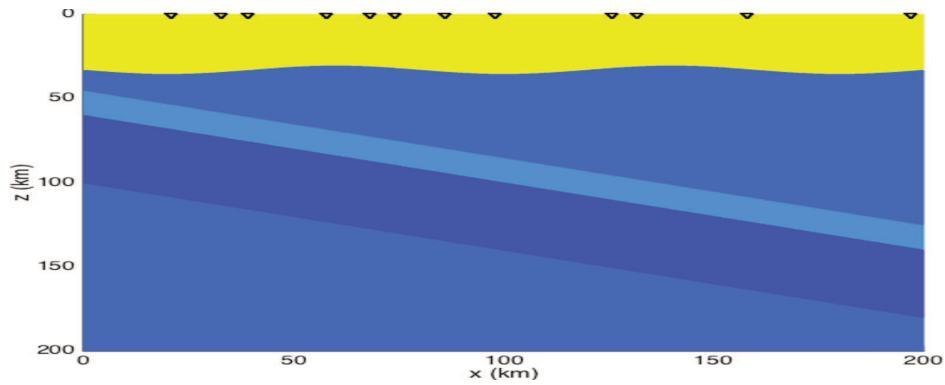\end{cases}
$$

Figure 8: Velocity model in Example 4.3. The black triangles indicate the receivers.
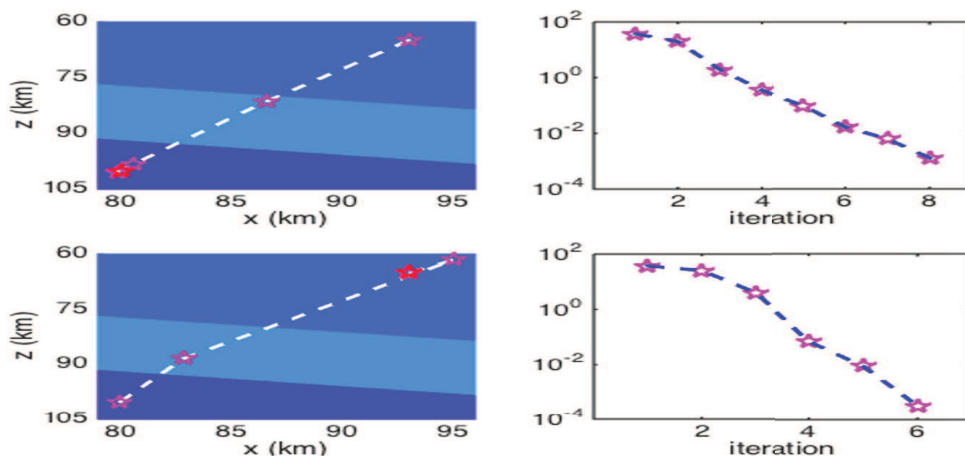

Figure 9: Convergent history of the first case in Example 4.3, from initial hypocenter in the subduction zone to the real hypocenter in the mantle (top) and its contrary case (bottom). Left: the convergent trajectories; Right: the absolute errors with respect to iteration step between the real and computed hypocenter of the earthquake.
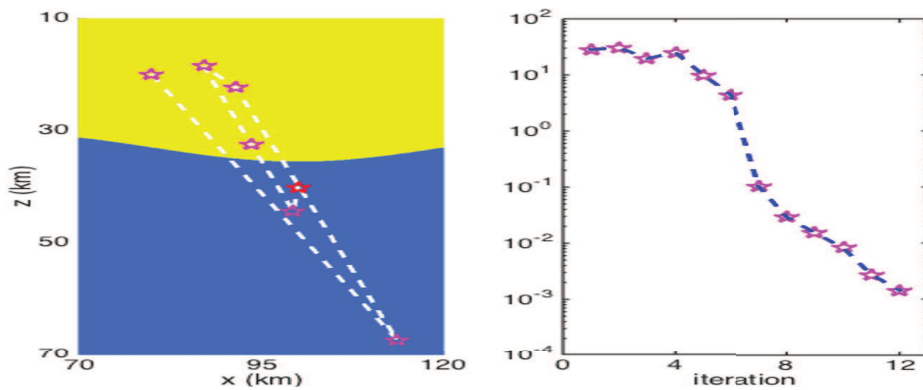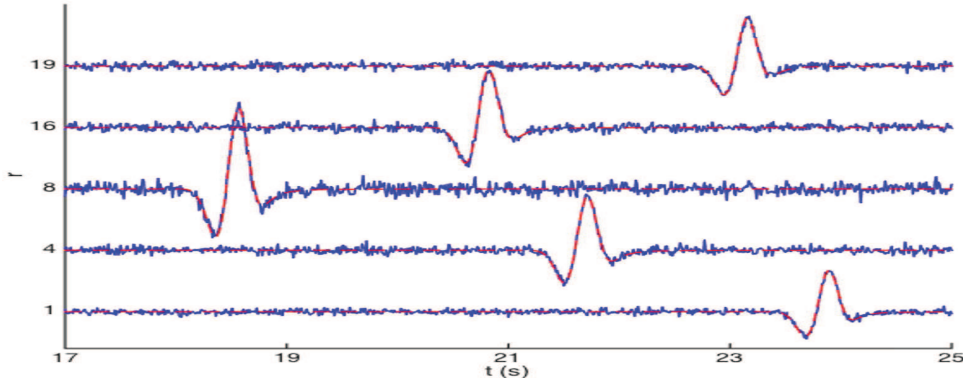

Figure 10: Convergent history of the second case in Example 4.3, from initial hypocenter in the crust to the real hypocenter in the mantle. Left: the convergent trajectory; Right: the absolute errors with respect to iteration step between the real and computed hypocenter of the earthquake.

Figure 11: Illustration of signal with noise in Example 4.4. The signal with noise $\widetilde{d}_r(t)$ (blue line) and the noise free signal $d_r(t)$ (red dashed line) for receivers $r=1,4,8,16,19$. The horizontal axis is the time t, and the longitudinal axis is the index of receiver r.

with unit 'km/s'. We consider the same set-up as in Example 4.2, e.g. the forward scheme, the boundary conditions, the discretized delta function and the receivers distribution. Considering the influence of the data noise and inaccurate velocity model, the inverse problem is solved by adding damping term. The detailed discussion can be found in Section 2.2 of [35].

In the first situation, we add noise

$$\widetilde{d}_r(t)=d_r(t)+N_r(t),$$

where $N_r(t)$ is subject to the normal distribution with the mean $\mu=0$ and the standard deviation

$$\sigma=5\%\times\max_t|d_r(t)|.$$

The signal with noise $\widetilde{d}_r(t)$ and the noise free signal $d_r(t)$ are illustrate in Fig. 11. Here the real earthquake hypocenter is $\xi_T=(50km,20km)$ and the origin time $\tau_T=10s$. Consider the initial earthquake hypocenter $\xi=(30km,10km)$ and the origin time $\tau=13s$, the convergent history is output in Fig. 12. Taking into account the effects of noise, it is not suitable to use the termination condition $\|\xi_k-\xi_{k+1}\|<\varepsilon$ as given in step 4 of the algorithm given in Subsection 3.3. Instead, we choose the hypocenter and origin time corresponding to the smallest value of the misfit function.

$$k_T=\operatorname*{argmin}_k\sum_{r\in\mathcal{A}}\chi_r(\xi_k,\tau_k).$$

Thus, the location result is (ξ_{k_T},τ_{k_T}). According to Fig. 12, the magenta pentagram is the final location result,

$$k_T=17,\quad \xi_{k_T}=(49.99km,19.78km),\quad \tau_{k_T}=10.03s.$$
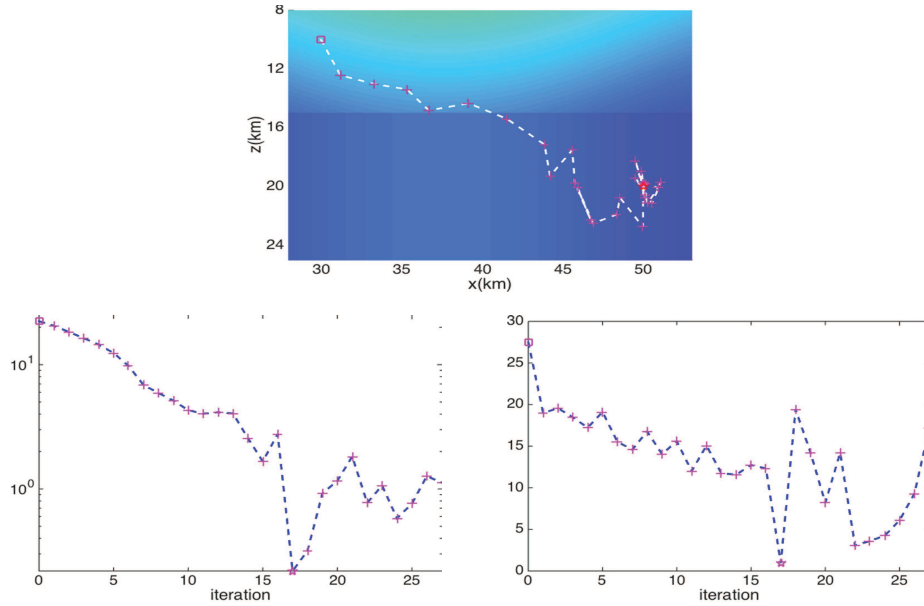
Figure 12: Convergent history of the first situation in Example 4.4. Top: the convergent trajectory; Bottom left: the absolute errors with respect to iteration step between the real and the computed hypocenter of the earthquake $\|\xi_k - \xi_T\|$; Bottom right: the value of the misfit function $\sum_{r \in \mathcal{A}} \chi_r(\xi_k, \tau_k)$. The magenta square is the initial hypocenter, the magenta plus denotes the hypocenter in the iterative process, the magenta pentagram indicate the smallest value of the misfit function, and the red pentagram is the real hypocenter.

In the bottom left of the figure, the absolute error between the numerical hypocenter and the real hypocenter is very small.

In the second situation, the real wave speed $\tilde{c}(x,z)$ is a perturbation of the known wave speed $c(x,z)$

$$\tilde{c}(x,z) = c(x,z) + N(x,z),$$

where $N(x,z)$ is subject to the normal distribution with the mean $\mu = 0$ and the standard deviation $\sigma = 5\% \times (6.2 + 0.2) = 0.32$. In Fig. 13, the velocity structures are presented. Here we want to test convergence effect when the velocity model is inaccurate. Similar to the previous discussion, we also choose the hypocenter and origin time corresponding to the smallest value of the misfit function. We can also observe the real signal $\tilde{d}_r(t)$ corresponding to the real wave speed $\tilde{c}(x,z)$ and the inaccurate signal $d_r(t)$ corresponding to the inaccurate velocity model $c(x,z)$ in Fig. 14. Consider the initial earthquake hypocenter $\xi = (30km, 10km)$ and the origin time $\tau = 13s$, the convergent history is output in Fig. 15. The magenta pentagram is the final location result,

$$k_T = 23, \quad \xi_{k_T} = (49.89km, 19.96km), \quad \tau_{k_T} = 9.99s.$$

And we can also observe a small absolute error between the numerical hypocenter and the real hypocenter. Based on the above discussions, we believe that our method can handle both data noise and inaccurate velocity model.
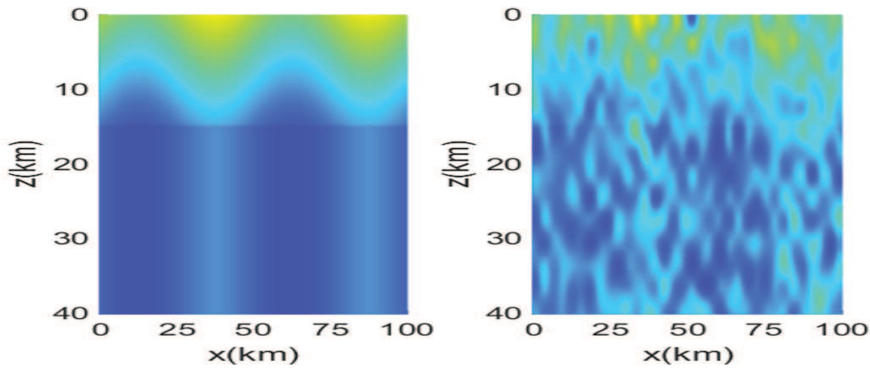
Figure 13: Inaccurate velocity model $c(x,z)$ (Left) and true velocity model $\widetilde{c}(x,z)$ (Right) in Example 4.4, the second situation.
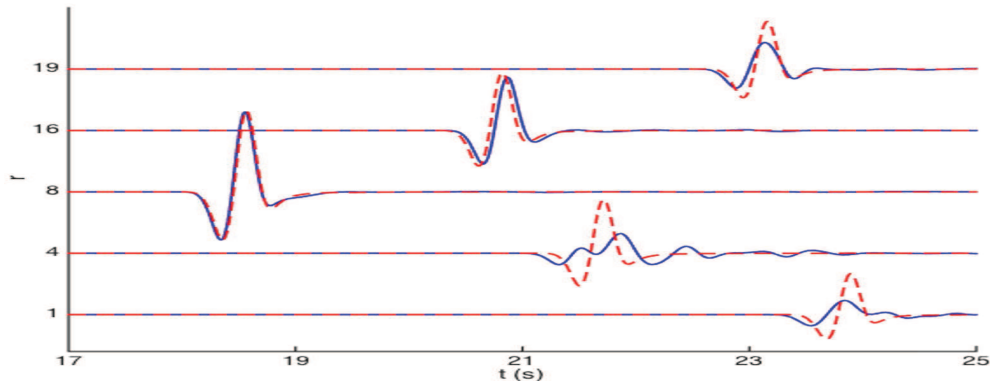

Figure 14: Illustration of signal with inaccurate velocity model in Example 4.4. The real signal $\widetilde{d}_r(t)$ (blue line) corresponding to the real wave speed $\widetilde{c}(x,z)$ and the inaccurate signal $d_r(t)$ (red dashed line) corresponding to the inaccurate velocity model $c(x,z)$ for receivers $r = 1,4,8,16,19$. The horizontal axis is the time t, and the longitudinal axis is the index of receiver r.

5   Conclusion and discussion

The main contribution in this paper is that convergence domain of the waveform based earthquake location method has been greatly expanded. Accordingly to the numerical evidence presented earlier, the convergence domain has been enlarged $5 \sim 100$ times in the two test problems. This means that even from the relatively poor initial values of earthquake hypocenter, our method is also likely to convergence to the correct results with high accuracy.

It should be noted that there are still many issues need to be further investigated: (a) We only use direct wave for inversion. It is of course very interesting to invert the earthquake parameters with other arrivals, e.g. the reflected wave. (b) Here, we deal with 2-D problem. For 3-D problem, we believe that the new method is also applicable. (c)
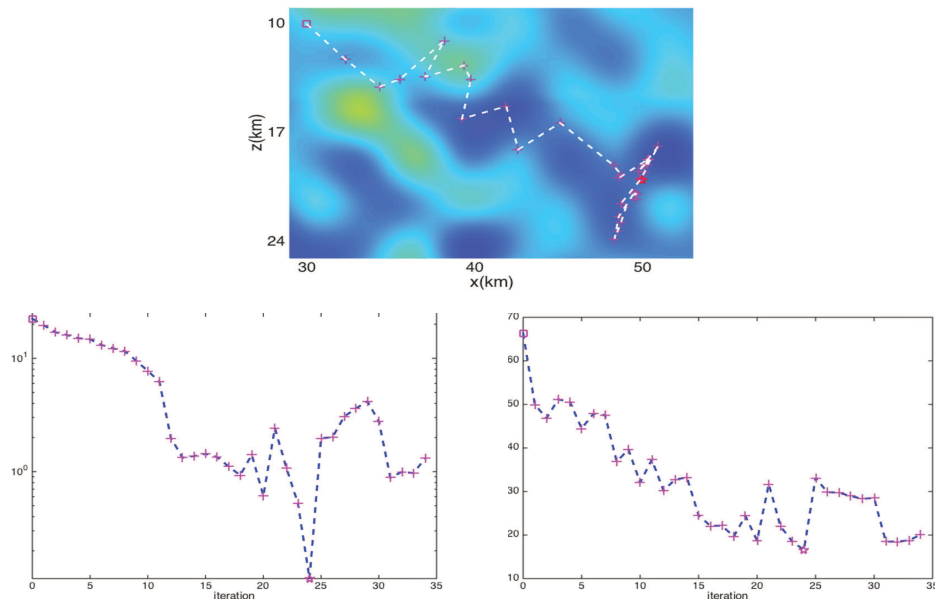
Figure 15: Convergent history of the second situation in Example 4.4. Top: the convergent trajectory; Bottom left: the absolute errors with respect to iteration step between the real and the computed hypocenter of the earthquake $\|\zeta_k - \zeta_T\|$; Bottom right: the value of the misfit function $\sum_{r \in \mathcal{A}} \chi_r(\zeta_k, \tau_k)$. The magenta square is the initial hypocenter, the magenta plus denotes the hypocenter in the iterative process, the magenta pentagram indicate the smallest value of the misfit function, and the red pentagram is the real hypocenter.

Although we considered the effects of noise and inaccurate velocity model, the practical data may be more complicated. Thus, we need to do more careful work. We hope these can be solved in the near future.

Acknowledgments

References

[1] H. Ammari, G. Bao and J.L. Fleming, An inverse source problem for maxwell's equations in magentoencephalography, *SIAM J. Appl. Math.*, **62**(4), 1369-1382, 2002.
[2] K. Aki and P.G. Richards, *Quantitative Seismology: Theory and Methods volume II*, W.H. Freeman & Co (Sd), 1980.

[3] T. Alkhalifah, Acoustic wavefield evolution as a function of source location perturbation, *Geophys. J. Int.*, **183**(3), 1324-1331, 2010.

[4] G. Bao, T.A. Ehlers and P.J. Li, Radiogenic Source Identification for the Helium Production-Diffusion Equation, *Commun. Comput. Phys.*, **14**(1), 1-20, 2013.

[5] G. Bao, J.S. Lin and F. Triki, A multi-frequency inverse source problem, *J. Differ. Equ.*, **249**, 3443-3465, 2010.

[6] M.A. Dablain, The application of high-order differencing to the scalar wave equation, *Geophysics*, **51**(1), 54-66, 1986.

[7] F.A. Dahlen, S.H. Hung and G. Nolet, Fréchet kernels for finite-frequency traveltimes - I. Theory, *Geophys. J. Int.*, **141**, 157-174, 2000.

[8] B. Engquist and B.D. Froese, Application of the Wasserstein metric to seismic signals, *Commun. Math. Sci.*, **12**(5), 979-988, 2014.

[9] B. Engquist and O. Runborg, Computational high frequency wave propagation, *Acta Numer.*, **12**, 181-266, 2003.

[10] B. Engquist, B.D. Froese and Y.N. Yang, Optimal transport for seismic full waveform inversion, *Commun. Math. Sci.*, **14**(8), 2309-2330, 2016.

[11] M.C. Ge, Analysis of source location algorithms Part I: Overview and non-iterative methods, *J. Acoust. Emiss.*, **21**, 14-28. 2003.

[12] M.C. Ge, Analysis of source location algorithms Part II: Iterative methods, *J. Acoust. Emiss.*, **21**, 29-51, 2003.

[13] L. Geiger, Probability method for the determination of earthquake epicenters from the arrival time only, *Bull. St. Louis Univ.*, **8**, 60-71, 1912.

[14] X.Y. Huang, D.H. Yang, P. Tong, J. Badal and Q.Y. Liu, Wave equation-based reflection tomography of the 1992 Landers earthquake area, *Geophys. Res. Lett.*, **43**, 1884-1892, 2016.

[15] S. Jin, H. Wu and X. Yang, Gaussian Beam Methods for the Schrödinger Equation in the Semi-classical Regime: Lagrangian and Eulerian Formulations, *Commun. Math. Sci.*, **6**(4), 995-1020, 2008.

[16] Y.H. Kim, Q.Y. Liu and J. Tromp, Adjoint centroid-moment tensor inversions, *Geophys. J. Int.*, **186**, 264-278, 2011.

[17] D. Komatitsch and J. Tromp, A perfectly matched layer absorbing boundary condition for the second-order seismic wave equation, *Geophys. J. Int.*, **154**, 146-153, 2003.

[18] W.H.K. Lee and S.W. Stewart, *Principles and Applications of Microearthquake Networks*, Academic Press, 1981.

[19] Y.Z. Lin and L.J. Huang, *Acoustic- and elastic-waveform inversion using a modified total-variation regularization scheme*, *Geophys. J. Int.*, **200**, 489-502, 2015.

[20] Q.Y. Liu and Y.J. Gu, Seismic imagine: From classical to adjoint tomography, *Tectonophysics*, **566-567**, 31-66, 2012.

[21] Q.Y. Liu, J. Polet, D. Komatitsch and J. Tromp, Spectral-Element Moment Tensor Inversion for Earthquakes in Southern California, *Bull. seism. Soc. Am.*, **94**(5), 1748-1761, 2004.

[22] R. Madariaga, Seismic Source Theory, in *Treatise on Geophysics (Second Edition)*, pp. 51-71, ed. Gerald, S., Elsevier B.V., 2015.

[23] I. Malyshev, An Inverse Source Problem for Heat Equation, *J. Math. Anal. Appl.*, **142**, 206-218, 1989.

[24] L. Métivier, R. Brossier, Q. Mérigot, E. Oudet and J. Virieux, Measuring the misfit between seismograms using an optimal transport distance: application to full waveform inversion, *Geophys. J. Int.*, **205**, 345-377, 2016.

[25] L. Métivier, R. Brossier, Q. Mérigot, E. Oudet and J. Virieux, An optimal transport ap-

proach for seismic tomography: application to 3D full waveform inversion, *Inverse Probl.*, **32**, 115008, 2016.

[26] A.F. Prugger and D.J. Gendzwill, Microearthquake location: A nonlinear approach that makes use of a simplex stepping procedure, *Bull. seism. Soc. Am.*, **78**, 799-815, 1988.

[27] N. Rawlinson, S. Pozgay and S. Fishwick, Seismic tomography: A window into deep Earth, *Phys. Earth Planet. Inter.*, **178**, 101-135, 2010.

[28] C. Satriano, A. Lomax and A. Zollo, Real-Time Evolutionary Earthquake Location for Seismic Early Warning, *Bull. seism. Soc. Am.*, **98**(3), 1482-1494, 2008.

[29] S.R. Tan and L.J. Huang, Reducing the computer memory requirement for 3D reverse-time migration with boundary-wavefield extrapolation method, *Geophysics*, **79**(5), S185-S194, 2014.

[30] C.H. Thurber, Nonlinear earthquake location: Theory and examples, *Bull. seism. Soc. Am.*, **75**(3), 779-790, 1985.

[31] C.H. Thurber, Earthquake, location techniques, in *Encyclopedia of Earth Sciences Series*, pp. 201-207, ed. Gupta, H.K., Springer, 2014.

[32] P. Tong, D.P. Zhao and D.H. Yang, Tomography of the 1995 Kobe earthquake area: comparison of finite-frequency and ray approaches, *Geophys. J. Int.*, **187**, 278-302, 2011.

[33] P. Tong, D.P. Zhao and D.H. Yang, Tomography of the 2011 Iwaki earthquake (M 7.0) and Fukushima nuclear power plant area, *Solid Earth*, **3**, 43-51, 2012.

[34] P. Tong, D. Zhao, D.H. Yang, X. Yang, J. Chen and Q. Liu, Wave-equation-based travel-time seismic tomography - Part 1: Method, *Solid Earth*, **5**, 1151-1168, 2014.

[35] P. Tong, D.H. Yang, Q.Y. Liu, X. Yang and J. Harris, Acoustic wave-equation-based earthquake location, *Geophys. J. Int.*, **205**(1), 464-478, 2016.

[36] J. Tromp, C. Tape and Q.Y. Liu, Seismic tomography, adjoint methods, time reversal and banana-doughnut kernels, *Geophys. J. Int.*, **160**, 195-216, 2005.

[37] F. Waldhauser and W.L. Ellsworth, A double-difference earthquake location algorithm: Method and application to the northern Hayward Fault, California, *Bull. seism. Soc. Am.*, **90**(6), 1353-1368, 2000.

[38] M. Warner and L. Guasch, Adaptive waveform inversion: Theory, *Geophysics*, **81**(6), R429-R445, 2016.

[39] X. Wen, High Order Numerical Quadratures to One Dimensional Delta Function Integrals, *SIAM J. Sci. Comput.*, **30**(4), 1825-1846, 2008.

[40] H. Wu and X. Yang, Eulerian Gaussian beam method for high frequency wave propagation in the reduced momentum space, *Wave Motion*, **50**(6), 1036-1049, 2013.

[41] D.H. Yang, M. Lu, R.S. Wu and J.M. Peng, An Optimal Nearly Analytic Discrete Method for 2D Acoustic and Elastic Wave Equations, *Bull. seism. Soc. Am.*, **94**(5), 1982-1991, 2004.